



## Co-registration of multi-sensor UAV imagery. Case study: Boreal forest areas

Patricio Martínez-Carricondo, Fernando Carvajal-Ramírez & Francisco Agüera-Vega

To cite this article: Patricio Martínez-Carricondo, Fernando Carvajal-Ramírez & Francisco Agüera-Vega (2022): Co-registration of multi-sensor UAV imagery. Case study: Boreal forest areas, Scandinavian Journal of Forest Research, DOI: [10.1080/02827581.2022.2084563](https://doi.org/10.1080/02827581.2022.2084563)

To link to this article: <https://doi.org/10.1080/02827581.2022.2084563>



Published online: 04 Jun 2022.



Submit your article to this journal [↗](#)



View related articles [↗](#)



View Crossmark data [↗](#)

RESEARCH ARTICLE



## Co-registration of multi-sensor UAV imagery. Case study: Boreal forest areas

Patricio Martínez-Carricondo <sup>a,b</sup>, Fernando Carvajal-Ramírez <sup>a,b</sup> and Francisco Agüera-Vega <sup>a,b</sup>

<sup>a</sup>Department of Engineering, Mediterranean Research Center of Economics and Sustainable Development (CIMEDES), University of Almería (Agrifood Campus of International Excellence, ceiA3). Almería, Spain; <sup>b</sup>Peripheral Service of Research and Development based on drones, University of Almería. Almería, Spain

### ABSTRACT

Monitoring the regeneration process of a forest is an important part of forestry management. Compared to traditional methods of counting tree species, UAVs have been a revolutionary means of saving time and costs due to the temporal and spatial flexibility of data collection. In turn, the integration of multispectral cameras allows the traditional vegetation indices that have been used with satellite imagery to be obtained. However, data from multispectral cameras must be combined with data from other types of sensors, such as RGB. It is therefore necessary to co-register all the information in order to obtain combined vegetation indices and carry out segmentation processes that allow the identification of the different tree species. In this study, the coordinate transformation methods available in QGIS software through the georeferencer plugin are evaluated. It also studies the influence of the number and distribution of control points on the accuracy of the transformation. It is concluded that of the transformation methods studied, TPS transformation has the highest accuracy with an MAE of 0.9 pixels and a deviation of 0.6 pixels, providing a minimum of 10 control points and a stratified or edge distribution.

### ARTICLE HISTORY

Received 5 April 2021  
Accepted 27 May 2022

### KEYWORDS

UAV-photogrammetry;  
multi-sensor imagery; co-  
registration; forest planning;  
forest inventory

### Introduction

Information on regeneration success is important in forest management. Furthermore, this information is required shortly after planting to carry out the supplementary measures if needed. Unmanned aerial vehicles (UAVs) may be particularly suitable for reforestation applications as they can collect very high-resolution data with great operational flexibility and a decrease in field survey costs.

Practitioners validate the regeneration success of replanted forest areas by assessing the adequacy of the spacing, survival, growth and species composition. These studies are carried out by manual counting in sampling plots (Feduck et al. 2018). If the condition, minimum height and seedling species within the sample cells used to conduct the establishment surveys could be derived from unmanned aerial vehicle images, then the reduced need for manual surveys could result in considerable cost savings. However, it is necessary to demonstrate that seedlings can be detected automatically or semi-automatically by remote sensing. The detection of seedlings requires extremely high spatial resolution images.

Other authors have already conducted similar studies, although for other purposes. For example, (Puliti et al. 2018) used automated procedures to detect small tree stumps and (Peña et al. 2015) to detect weed seedlings in bare soil in an agricultural application. (Hall & Aldred 2014) detected only 44% of seedlings with a crown diameter of less than 30 cm using a 1:500 scale and colour and infrared

photographs. More recently, (Goodbody et al. 2018) classified 2.4 cm spatial resolution images of red, green and blue (RGB), which were acquired by a UAV on harvest blocks replanted five to 15 years earlier in British Columbia, Canada, and obtained user accuracies for conifer coverage between 35% and 97%. However, no attempt was made to detect the individual seedlings of conifers, which in their study area were more than 1 m high. These authors recognized that the potential for detecting all stems using aerial remote sensing technologies is still limited and calls for more research. As another example, (Hentz et al. 2018) built a toolbox in ArcGIS for tree identification that was tested in three areas with Eucalyptus, Pinus and broadleaved trees with satisfactory results, but less accurate in natural forests. Depending on the spatial resolution of the images, seedling detection is similar to the detection of individual trees in mature forests, which has been well studied using satellites (Agarwal et al. 2013; Gomes and Maillard 2016), pilot planes (Gougeon 1995; Wulder et al. 2000; Franklin et al. 2003; Pouliot et al. 2005; Wolf and Heipke 2007; Ke and Quackenbush 2011; Leckie et al. 2017), airborne laser scanning data (Vauhkonen et al. 2012) and, more recently, UAVs (Fritz et al. 2013; Wallace et al. 2014; Wallace et al. 2014; Jaskierniak et al. 2015; Puliti et al. 2015; Kang et al. 2017; Nevalainen et al. 2017; Panagiotidis et al. 2017). With fixed spatial resolution, the accuracy with which individual trees are detected tends to improve with crown size (Pouliot et al. 2005). For example, using 15 cm resolution multispectral airborne

images and an image segmentation algorithm, (Hirschmugl et al. 2007) obtained 70% accuracy in replanted conifers between five and 10 years of age with an average height of 138 cm.

Recently, UAVs have enabled the use of a large variety of sensors with the capacity for close range sensing and are applied in regenerating forests (Chen et al. 2017; Hird et al. 2017). Digital cameras operating in the visible spectrum are used for UAV-photogrammetric projects combined with the Structure from Motion (SfM) (Fonstad et al. 2013) and multi-view stereopsis (MSV) (Furukawa and Ponce 2010) techniques, producing very high-resolution orthoimages and Digital Elevation Models (DEMs), as well as very dense point clouds of the terrain. The absolute georeferencing of the photogrammetric project can be obtained directly through the EXIF data stored in the photographs, or indirectly through the use of ground control points (GCPs). This second way has traditionally been widely used but it is usually very laborious and time consuming, sometimes even dangerous due to the inaccessibility of the working area (Agüera-Vega et al. 2017; Martínez-Carricondo et al. 2018). This is why, in forested and large areas, it is interesting to carry out a direct georeferencing of the photogrammetric project.

When the UAV sensor includes multispectral images, all the indices designed for satellite imagery can be applied or adapted to UAV applications.

However, the multispectral cameras that are available for mounting on a UAV do not have a high geometric resolution, so it is often necessary to obtain the RGB orthoimage using another camera of higher resolution. When different sensors are used, the EXIF data of the photographs taken are different (due to the fact that each sensor incorporates its own Global Navigation Satellite System, GNSS), which means that the direct georeferencing of the photogrammetric project is also different. Therefore, the orthoimages from the multispectral camera and the orthoimage from the RGB camera do not have an exact match (Turner et al. 2014; Dias et al. 2019). Thus, the band misregistration effect is a problem when obtaining indices based on RGB camera products and multispectral camera products. It is therefore necessary to co-register all the available bands in order to combine them to obtain the desired indices.

Image registration is a technique for transforming a distorted image to a reference image so that an image overlay analysis can be performed (Brown 1992). In general, image registration contains four main steps, namely feature extraction, feature matching, image transformation and image interpolation (Dawn et al. 2010). Co-registration can be carried out by georeferencing through different typical transformation methods (Boutoura and Livieratos 2006). Second-degree polynomial transforms have been frequently used to georeference old maps (Cajthaml 2011; Brigante and Radicioni 2014; Follin et al. 2016) as well as Helmert transformations when no deformations are to be introduced in georeferencing (Boutoura and Livieratos 2006). More complex transformation methods based on thin plate spline (TPS) for image registration have also been used (Sprenkel et al. 1997; Donato and Belongie 2002; Bartoli et al. 2010)

as well as more sophisticated methods for georeferencing satellite images (Willneff et al. 2008; Widyaningrum et al. 2016) and even multispectral images from UAVs (Jhan et al. 2016).

The aim of this research is to evaluate the accuracy obtained with the classical transformation methods provided by a geographic information system (GIS) for the co-registration of the four bands coming from a multispectral camera, taking as a reference the RGB orthoimage obtained by a different camera of higher resolution. For this purpose, different transformation methods and different combinations and distributions of control points are established. By completing this research, conclusions will be drawn to obtain a quick and easy co-registration of the images from different sensors in order to obtain indices that allow the identification of different tree species, which will be addressed in forthcoming publications.

## Materials and methods

The methods used to carry out this research are summarised in Figure 1.

### Study site

The study area was located in Innlandet county, south-eastern Norway (Figure 2).

The total surface of the study area was 8.4 ha, and it was divided into 20 subzones. The average elevation of the study area was 270 m over the sea level ranging from 260 to 278 m, and the average slope was 9%. Most of the study area is free of high vegetation as it has been cut down in the last five years. The study site is currently undergoing a process of natural reforestation. The main species found are conifers, *Picea Abies* and *Pinus Sylvestris* and non-conifers such as Birch. The largest sizes found are around 100 cm in height, although the majority of the species are under 25 cm. Figure 3 shows an example of each of the main species.

### UAV and sensor

The images used in this work were taken using a rotatory wing DJI Phantom 4 Pro UAV with four rotors. This equipment has a navigation system using GPS and GLONASS. In addition, it is equipped with a front, rear and lower vision system that allows it to detect surfaces with a defined pattern and adequate lighting and avoid obstacles with a range between 0.2 and 7 m.

The UAV was equipped with a RGB camera mounted on a motion-compensated three-axis gimbal and a Parrot Sequoia multispectral camera mounted on a 3D printed bracket (Figure 4).

The Phantom 4 RGB camera (Figure 5a) is equipped with a 1-inch 20-megapixel (5472 × 3648) sensor, and it has a manually adjustable aperture from F2.8 to F11. The lens have a fixed focal length of 8.8 mm and a horizontal FOV of 84°.

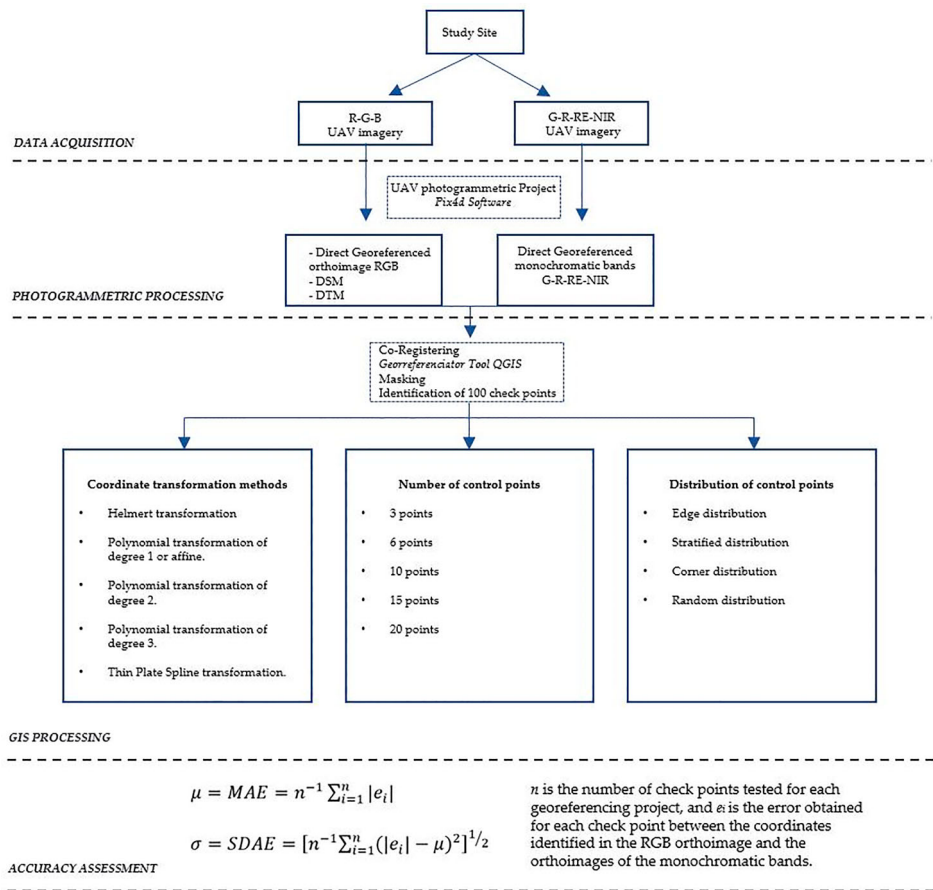


Figure 1. Flowchart of the methodology used in this work.

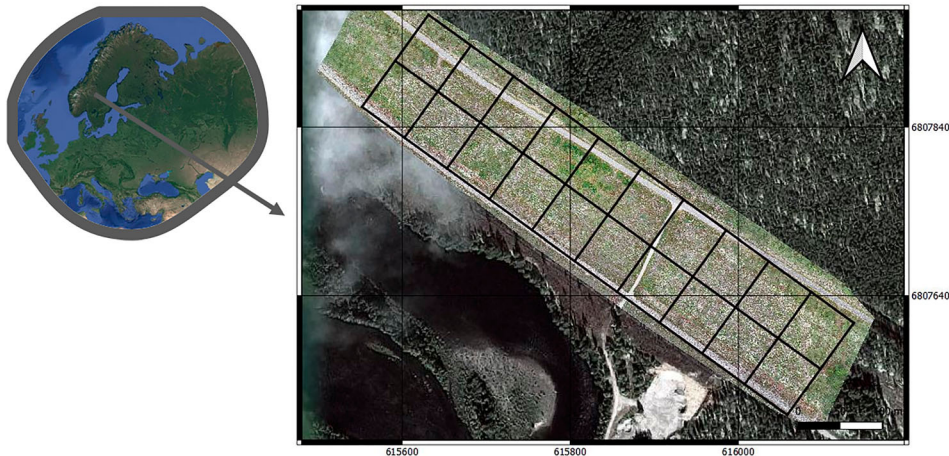


Figure 2. Location of the study area. The coordinates are referred to UTM Zone 32 N (WGS84).

The average ground sample distance (GSD) was 1.2 cm, corresponding to a flight height of 45 m.

The Parrot Sequoia camera (Figure 5b) has four sensors with a resolution of 1.2 megapixels (1280 × 960) that collect multispectral imagery by employing a global shutter in the green, red, red-edge and near-infrared wavelengths. The four lenses have a fixed focal length of 4 mm and a horizontal and vertical FOV of 61.9° and 48.5°, respectively. Furthermore, the camera includes an integrated high-resolution RGB

sensor of 16 megapixels (4608 × 3456) and a rolling shutter, which can be useful for the UAV photogrammetric process.

One of the most interesting characteristics of this multispectral camera is that it is equipped with an irradiance sensor to record light conditions in the same spectral bands as the multispectral sensor and at the same time as the flights. Thanks to this device, light changes throughout the time of flight can be compensated by calculating the absolute reflectance during post-processing.



**Figure 3.** Main species in the study site. (a) *Picea Abies*; (b) *Pinus Sylvestris*; (c) Non-Conifers (Birch).



**Figure 4.** Unmanned Aerial Vehicle (UAV) system used in this work.

### *Flight route planning and image acquisition*

The flight was carried out with an autopilot using the DJI GS Pro © application for the purpose of obtaining nadiral photographs. Figure 6 shows some of the parameters configured for the flight execution. Due to the low slope of the zone, the flight altitude was set at a constant distance of 45 m above ground level, which implies an equivalent

ground sample distance of 1.2 and 4.5 cm for the RGB and multispectral images, respectively – the reason why this flight height was selected. In accordance with the flight altitude, the UAV speed and the light conditions at the time of flight, the shutter speed was adjusted to minimise the effect of blurring on the images taken. The flight plan consisted of 16 passes, and a total of 460 and 460 (x4 bands) images for the RGB and multispectral cameras, respectively, were selected to carry out the photogrammetric project. Both the RGB camera and the multispectral one were triggered every three seconds, and the flight speed was set to obtain forward and side overlaps of 75% and 60%, respectively, which were calculated for the RGB camera. Larger image overlaps are justified by the presence of a large density of high trees in order to have a greater depth in the point cloud obtained after the photogrammetric process (Dandois et al. 2015). However, in this case it is possible to reduce the overlaps between images for reducing flight time and computational process (Domingo et al. 2019).

### *Photogrammetric processing*

The RGB and multispectral photogrammetric projects were processed using Pix4Dmapper Pro version 3.1.23, a software



**Figure 5.** Cameras used in this work: (a) Phantom 4 RGB camera; (b) Parrot Sequoia camera and sunshine sensor.

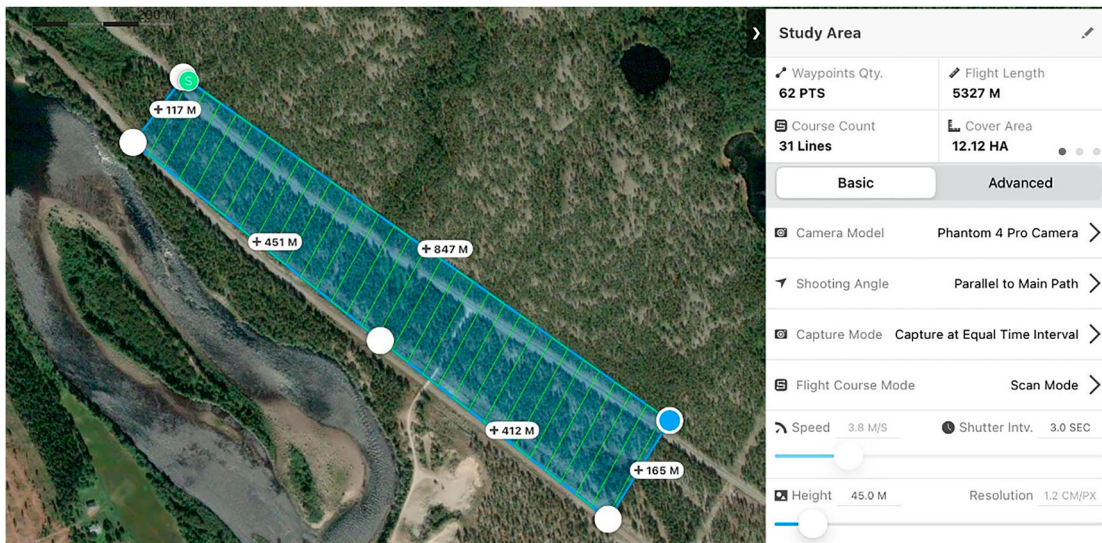


Figure 6. Flight path configuration with DJI GS Pro © software.

application based on the SfM and MVS algorithms, which allows a significant reduction in the computing time required for most of the processes involved in UAV multispectral photogrammetric projects. Both projects were processed independently. After previous quality checking of the imagery acquired by the sensor in a complete flight mission, the internal calibration parameters and coordinates of the image principal points of all the images were loaded from the EXIF data and considered as initial data for the iterative process of block adjustment. Sets of tie points in the overlapped areas of the images were automatically identified by autocorrelation algorithms. It was checked that the number of overlapping images computed for each pixel of the resulting orthomosaic was sufficient to match a large number of tie points throughout the study area. The bundle block adjustment process depends directly on the number of 2D and 3D keypoint observations.

The internal camera parameters, including the radial and decentring distortion coefficients, the focal length and the principal point coordinates, were optimised by an iterative field camera calibration process for each of the four sensors included in the multispectral camera.

Manual identification of the GCPs coordinates in the images made it possible to assign the absolute geolocation of the photogrammetric block. However, for the purpose of tree counts, high precision absolute georeferencing is not necessary. That is why the GCPs were not used prior to the photogrammetric flight. Therefore, direct georeferencing has been carried out based on the geographic coordinates extracted from the EXIF data of each photograph.

Finally, some products were obtained from the photogrammetric projects based on the triangular irregular network (TIN) resulting from the densified terrain point cloud. These are the Digital Surface Model (DSM) with a resolution of 1 x GSD, the Digital Terrain Model (DTM) with a resolution of 5 x GSD, a dense point cloud and an RGB orthoimage, and monochromatic reflectance orthorectified images corresponding to each of the four channels.

### Co-registration of multispectral bands and RGB orthoimage

Once the RGB orthophoto and orthophotos for each of the four monochromatic bands have been obtained, they can be used to extract vegetation indexes, for example a normalised difference vegetation index (NDVI) (Rouse et al. 1974) to help identify the different tree species present in the study area. However, the georeferencing of each of these orthophotos do not match as they have been obtained from different sensor photographs. This is also true for the four bands of the multispectral camera; however, processing with the Pix4d software reduces this misregistration effect to below one pixel. Therefore, the first essential step is the co-registration of the RGB orthophoto with the orthophotos of the four monochromatic bands. Figure 7a shows an example of a displacement between the RGB orthophoto and the monochromatic red band.

To quantify the average displacement between the RGB orthophoto and the orthophotos of the four monochromatic bands, 100 check points were established throughout the study area. The result of this quantification resulted in a mean absolute error (MAE) (Willmott and Matsuura 2005) of 56.18 pixels (taking as reference the pixel of the monochromatic bands) and a standard deviation of this error (SDAE) of 6.36 pixels. Figure 7b shows the error measured at 100 check points distributed throughout the study area.

The co-registration of the orthophotos has been carried out through the geographic information system (GIS) QGIS 3.10. This tool is open source software for GNU/Linux, Unix, Mac OS, Microsoft Windows and Android platforms. It allows the handling of raster and vector formats through the GDAL and OGR libraries as well as through databases. The process has been carried out using the QGIS software's "georeferencing" tool. This tool allows the raster to be referenced to geographic or projected coordinate systems by creating a new GeoTIFF or by adding a reference file to the existing image. The basic approach to georeferencing a

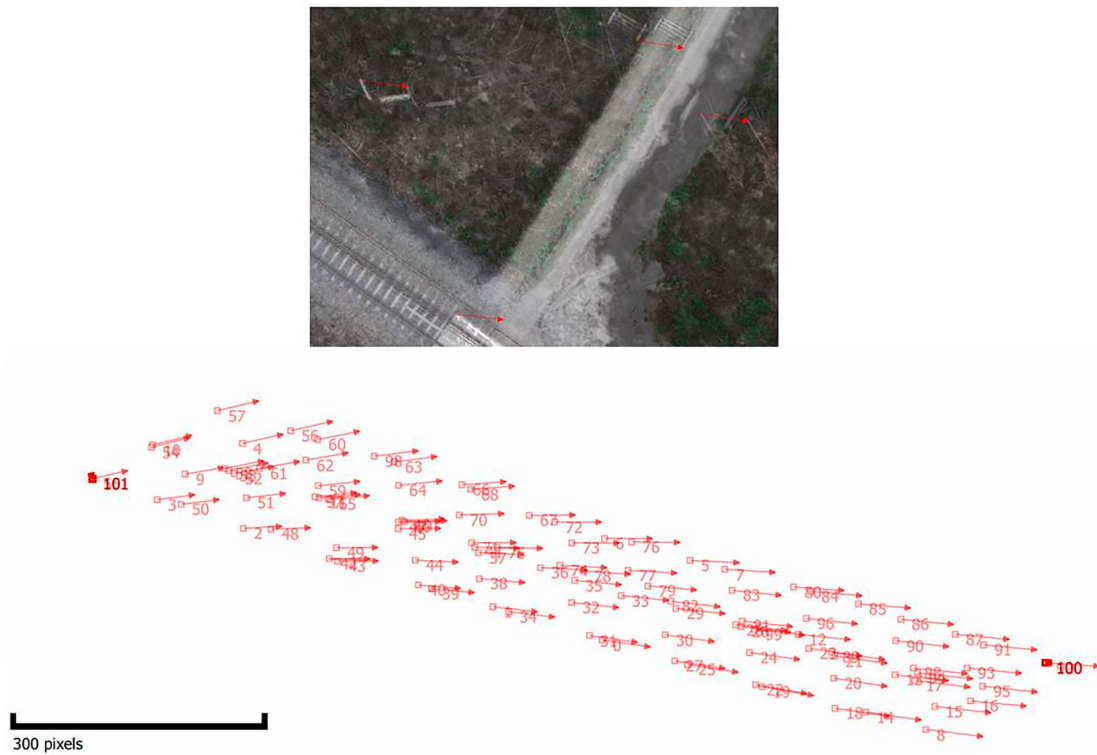


**Figure 7.** (a) Examples of displacements between the RGB orthophoto and the monochromatic red band (both layers appear overlapping and using 70% transparency in the monochromatic band); (b) Displacements measured at 100 check points distributed throughout the study area.

raster is to locate points on the raster for which the coordinates can be accurately determined. The usual procedure for georeferencing an image is to select multiple points on the raster, which specifies their coordinates, and choose a suitable transformation type. In our case, the four monochromatic bands have been georeferenced based on the RGB orthoimage.

The tool has different types of transformations according to the mathematical model used. The types of transformation that have been tested in this study are as follows:

- Helmert transformation
- Polynomial transformation of degree 1 or affine
- Polynomial transformation of degree 2
- Polynomial transformation of degree 3
- Thin plate spline transformation

Depending on the type of transformation chosen, a certain number of control points are required for the mathematical model to have a solution. If more control points are used than strictly necessary, the tool performs a least squares bundle adjustment to minimise the error.

### Helmert transformation

The Helmert or 2D similarity transformation model corresponds to a conformal transformation that keeps all angles and changes all distances by the same amount. This type of transformation considers three factors: the rotation, translation and scale. In addition, in order to be able to apply this type of transformation, the coordinates of two control

points in both systems are needed to mathematically solve the four parameters of the transformation (Pérez 2001). The mathematical model is expressed by the equation (1).

$$\begin{bmatrix} X \\ Y \end{bmatrix} = k \cdot \begin{bmatrix} \cos \theta & -\sin \theta \\ \sin \theta & \cos \theta \end{bmatrix} \cdot \begin{bmatrix} x \\ y \end{bmatrix} + \begin{bmatrix} T_x \\ T_y \end{bmatrix} \quad (1)$$

where:

$x, y$  are the coordinates of a point corresponding to the initial plane.

$X, Y$  are the adjusted coordinates of a point corresponding to the transformed plane.

$k$  is the scaling factor.

$\theta$  is the angle of rotation.

$T_x, T_y$  are the translations on the  $x$  and  $y$  axes.

### Polynomial transformation of degree 1 or affine

The two-dimensional (2D) affine transformation model (P1) corresponds to a transformation that considers the non-orthogonality of the transformed axes and establishes different scaling factors for each direction of the corresponding axis (abscissa and ordinate axis direction). In the case of this type of transformation, the coordinates of three control points in both systems are needed to mathematically solve the six parameters of the transformation (Pérez 2001). The mathematical model is expressed by

equation (2).

$$\begin{bmatrix} X \\ Y \end{bmatrix} = \begin{bmatrix} \cos \theta & -\sin \theta \\ \sin \theta & \cos \theta \end{bmatrix} \begin{bmatrix} 1 & -\sin \beta \\ 0 & \cos \beta \end{bmatrix} \begin{bmatrix} \lambda_x \cdot x \\ \lambda_y \cdot y \end{bmatrix} + \begin{bmatrix} T_x \\ T_y \end{bmatrix} \quad (2)$$

where:

$x, y$  are the coordinates of a point corresponding to the initial plane.

$X, Y$  are the adjusted coordinates of a point corresponding to the transformed plane.

$\lambda_x$  is the scaling factor in the x-axis direction.

$\lambda_y$  is the scaling factor in the y-axis direction.

$\theta$  is the angle of rotation.

$\beta$  is the angle of non-perpendicularity between the x-axis and y-axis.

$T_x, T_y$  are the translations on the x and y axes.

The mathematical model can also be expressed according to equation (3).

$$\begin{bmatrix} X \\ Y \end{bmatrix} = \begin{bmatrix} a_0 + a_1 \cdot x + a_2 \cdot y \\ b_0 + b_1 \cdot x + b_2 \cdot y \end{bmatrix} \quad (3)$$

where:

$x, y$  are the coordinates of a point corresponding to the initial plane.

$X, Y$  are the adjusted coordinates of a point corresponding to the transformed plane.

$a_0, a_1, a_2, \dots, b_0, b_1, b_2, \dots, b_n$  are the polynomial transformation parameters to be determined.

### Polynomial transformation of degree 2

The polynomial transformation of degree 2 (P2) is a type of transformation that does not preserve collinearity as it introduces curvature into the transformation. It also does not maintain parallelism or angles. It is considered a high accuracy transformation but has loss of reliability outside the common area of fit between the two systems. In two-dimensional space, it requires the use of six control points in order to mathematically solve the 12 parameters of the transformation (Pérez 2001). The mathematical model is expressed by equation (4).

$$\begin{bmatrix} X \\ Y \end{bmatrix} = \begin{bmatrix} a_0 + a_1 \cdot x + a_2 \cdot y + a_3 \cdot xy + a_4 \cdot x^2 + a_5 \cdot y^2 \\ b_0 + b_1 \cdot x + b_2 \cdot y + b_3 \cdot xy + b_4 \cdot x^2 + b_5 \cdot y^2 \end{bmatrix} \quad (4)$$

where:

$x, y$  are the coordinates of a point corresponding to the initial plane.

$X, Y$  are the adjusted coordinates of a point corresponding to the transformed plane.

$a_0, a_1, a_2, \dots, b_0, b_1, b_2, \dots, b_n$  are the polynomial transformation parameters to be determined.

### Polynomial transformation of degree 3.

In this case, the use of 10 control points is required to mathematically solve the 20 parameters of the polynomial transformation of degree 3 (P3). The mathematical model is

expressed by equation (5).

$$\begin{bmatrix} X \\ Y \end{bmatrix} = \begin{bmatrix} a_0 + a_1 \cdot x + a_2 \cdot y + a_3 \cdot xy + a_4 \cdot x^2 + a_5 \cdot y^2 + a_6 \cdot yx^2 \\ + a_7 \cdot xy^2 + a_8 \cdot x^3 + a_9 \cdot y^3 \\ b_0 + b_1 \cdot x + b_2 \cdot y + b_3 \cdot xy + b_4 \cdot x^2 + b_5 \cdot y^2 + b_6 \cdot yx^2 \\ + b_7 \cdot xy^2 + b_8 \cdot x^3 + b_9 \cdot y^3 \end{bmatrix} \quad (5)$$

where:

$x, y$  are the coordinates of a point corresponding to the initial plane.

$X, Y$  are the adjusted coordinates of a point corresponding to the transformed plane.

$a_0, a_1, a_2, \dots, b_n$  are the polynomial transformation parameters to be determined.

### Thin plate spline transformation.

The thin plate spline (TPS) is an effective tool for representing coordinate mappings in two dimensions. The method has been successfully applied in several disciplines. For example, (Bookstein 1989) studied its use for modelling changes in biological shapes. (Pedersen 2000) applied the TPS transformation to estimate the positions of protein spots in 2D electrophoresis gels. To understand the mathematical properties of splines in a simpler way, it is often common to make analogies based on mechanical behaviour. In this case, a flat, elastic plate subjected to internal forces caused by a series of external forces is considered (Keller and Borkowski 2019). Unfortunately, the solution requires the inversion of a  $p \times p$  matrix, where  $p$  is the number of points in the dataset, which makes it impractical for large-scale applications. However, it is possible to obtain a high-quality approximate solution using only a small subset of corresponding points (Donato and Belongie 2002). Once the mathematical model is developed, the TPS value of any point can be calculated based on equation (6).

$$f(x, y) = \sum_{i=1}^n \lambda_i r_i^2 \ln r_i + d_{00} + d_{10}x + d_{01}y \quad (6)$$

where  $\lambda_i, d_{00}, d_{10}, d_{01}$  are the parameters of the TPS transformation.

### Combination of georeferencing projects analysed based on the number and distribution of control points

In order to assess the accuracy of each of the five types of transformation in the previous section, four different types of control-point distribution have been established:

- (1) In the edge distribution, the control points are placed around the edge of the study area.
- (2) In the stratified distribution, the control points are placed in a stratified way.
- (3) In the corner distribution, the control points are placed in the corners of the study area.
- (4) In the random distribution, the control points are placed randomly throughout the study area.



In addition, the performance has been analysed as a function of the number of control points used in the transformation. Thus, the accuracy has been studied using three, six, 10, 15 and 20 control points. In order to obtain the average values, each of the above cases was repeated five times. Bearing in mind that the second-degree polynomial transformation requires a minimum of six control points and that the third-degree polynomial transformation requires a minimum of 10 control points. The total number of georeferencing projects studied was 5 (transformation types)  $\times$  4 (distribution types)  $\times$  5 (combinations of control points)  $\times$  5 (repeats) = 60 = 440 georeferencing projects.

For all the combinations, the resampling method chosen was that of the “nearest neighbour” as changing the statistics of the image was not desired.

The points identified were distributed homogeneously throughout the study area. For this purpose, the study area was divided into 20 sub-zones, and five points were identified in each sub-zone. Of all the points identified, a certain number was used to perform the transformation (control points), and the rest were used to assess the accuracy of the georeferencing (check points). Figure 8 shows all the identified points on the RGB orthophoto and the monochromatic bands.

### Accuracy assessment

The accuracy of all the georeferencing projects was evaluated using the identified points that had not been used for georeferencing (check points) using the MAE and SDAE formulation. To this end, the check points were identified in the orthoimage of the monochromatic band, and their coordinates were compared with the same point identified in the RGB orthoimage. The formulation used is shown in equations (7) and (8).

$$\mu = MAE = n^{-1} \sum_{i=1}^n |e_i| \quad (7)$$

$$\sigma = SDAE = \left[ n^{-1} \sum_{i=1}^n (|e_i| - \mu)^2 \right]^{\frac{1}{2}} \quad (8)$$

where  $n$  is the number of check points tested for each georeferencing project, and  $e_i$  is the error obtained for each check point.

### Results

Figures 9–12 show the MAE and SDAE averages for the five replicates that were conducted. The abscissa axis shows the

number of control points used to carry out the coordinate transformation. The ordinate axis represents the error obtained in the transformation expressed in pixels, which refers to the orthoimage of the monochromatic band. For each type of transformation, the trend of the average MAE for each of the five types of transformation is plotted as a function of the number of control points used. In turn, for each number of control points used, the average SDAE obtained in the five repetitions of each type of transformation is represented by a vertical bar. In order to restrict the study to high-precision cases, the abscissa axis is restricted to values between 0 and 10 pixels.

Figure 9 represents the results obtained for the edge distribution georeferencing projects. Thus, for the Helmert transformation, the average MAE varies from 2.7 pixels for three control points to 2.0 pixels for 20 control points, with a deviation of the result varying from 1.2 pixels for three control points to 1.1 pixels for 20 control points. For the P1 transformation, the average MAE varies between 2.9 pixels for three control points and 2.0 pixels for 20 control points, and the deviation varies between 1.6 and 1.1 pixels for three and 20 control points, respectively. For the P2 transformation, the average MAE varies between 4.3 pixels for six control points and 2.2 pixels for 20 control points, with the deviation varying between 2.5 and 1 pixel. For the P3 transformation, the average MAE varies between 6.4 pixels for 10 control points and 4.1 pixels for 20 control points, and the deviation varies between 4.4 and 2.6 pixels. For the TPS transformation, the average MAE varies between 2.9 pixels for three control points and 1 pixel for 20 control points, with the deviation varying between 1.6 and 0.6 pixels.

Figure 10 represents the results obtained for the stratified distribution georeferencing projects. Thus, for the Helmert transformation, the average MAE varies from 2.3 pixels for three control points to 2.2 pixels for 20 control points, with a deviation of the result varying from 1.4 pixels for three control points to 1.3 pixels for 20 control points. For the P1 transformation, the average MAE varies between 3.2 pixels for three control points and 2.1 pixels for 20 control points, and the deviation varies between 2.0 and 1.3 pixels for three and 20 control points, respectively. For the P2 transformation, the average MAE varies between 4.7 pixels for six control points and 2.6 pixels for 20 control points, with the deviation varying between 2.9 and 2.5 pixels. For the P3 transformation, the average MAE varies between 14.0 pixels for 10 control points and 9.6 pixels for 20 control points, and the deviation varies

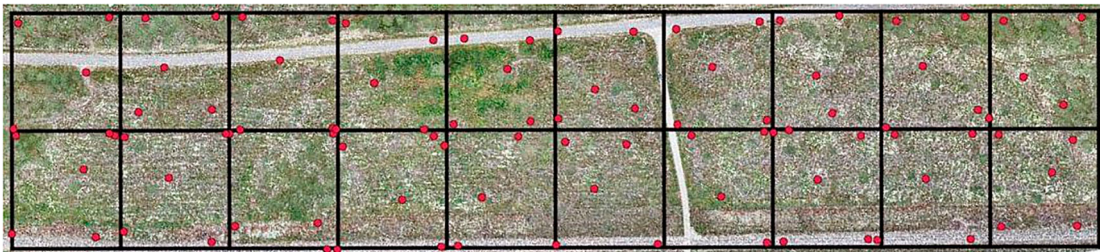


Figure 8. Distribution of identified points on the RGB orthophoto.

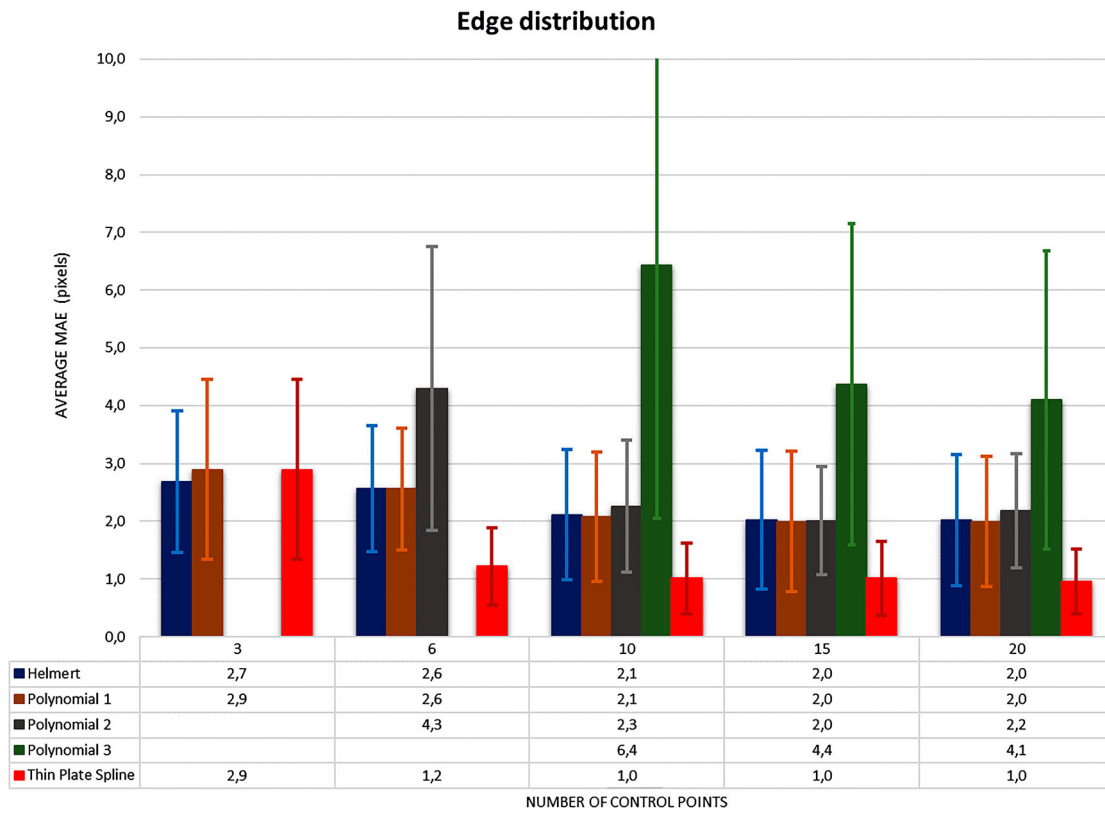


Figure 9. Average MAE and SDAE results for edge distribution georeferencing projects.

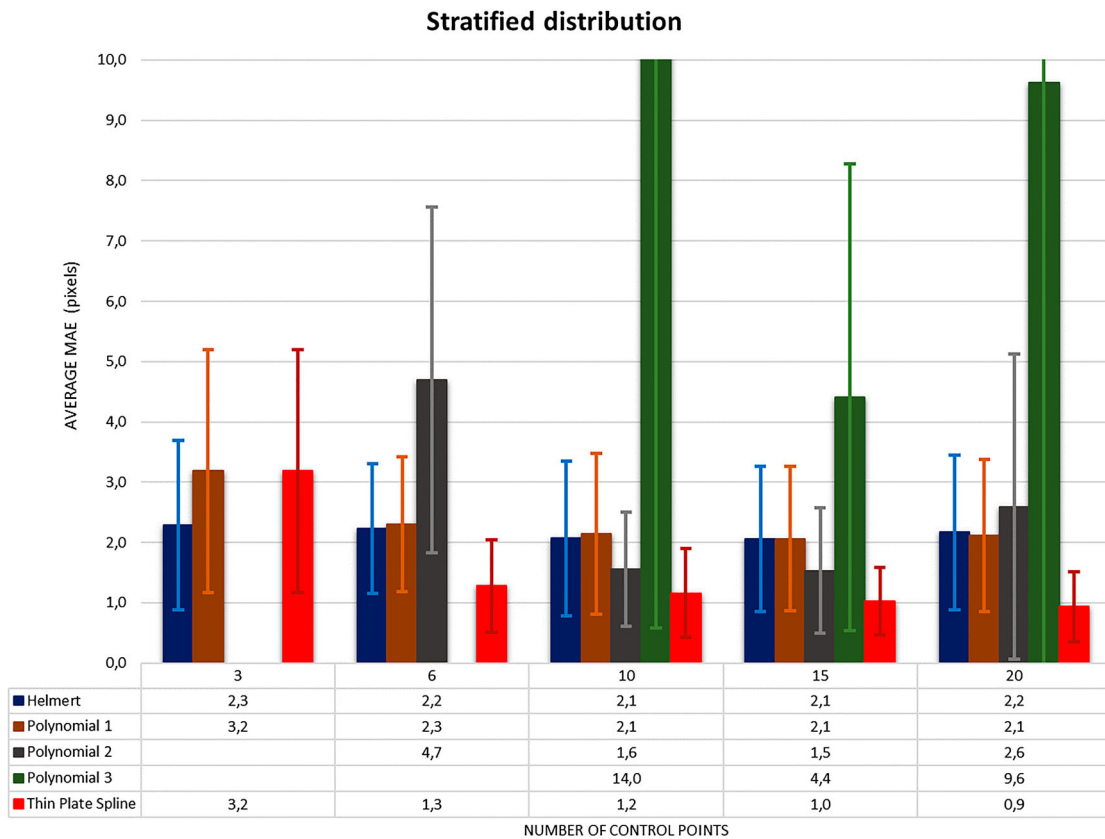


Figure 10. Average MAE and SDAE results for stratified distribution georeferencing projects.

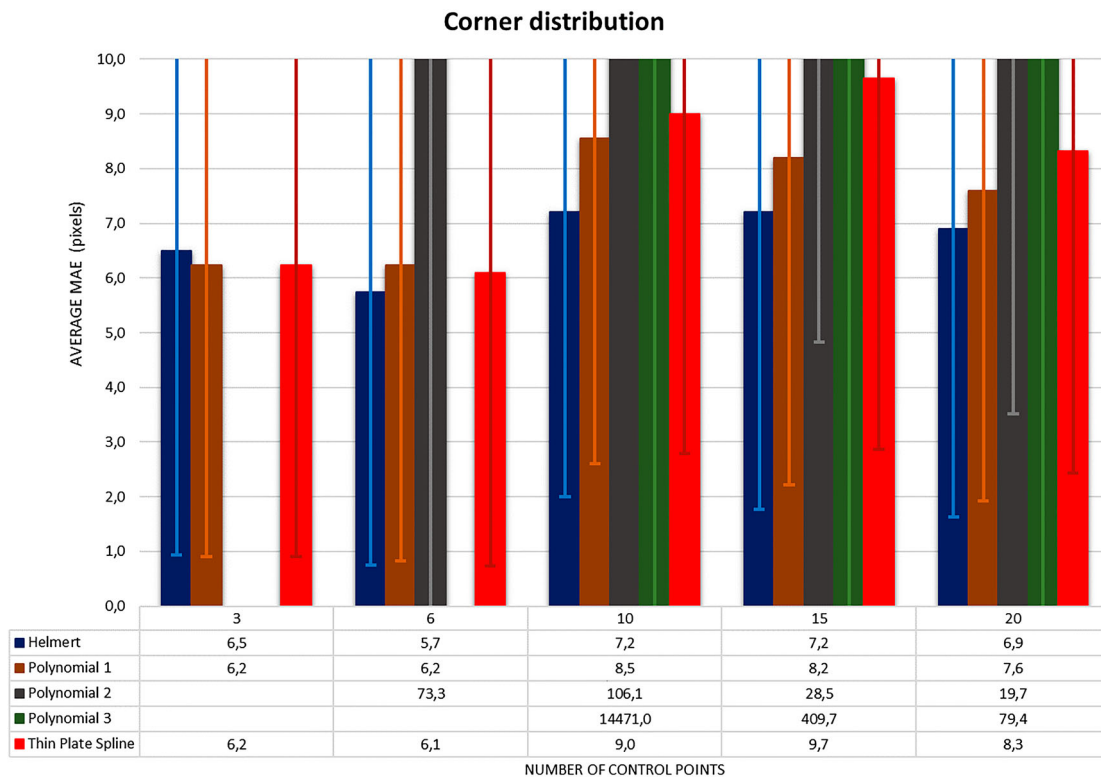


Figure 11. Average MAE and SDAE results for the corner distribution georeferencing projects.

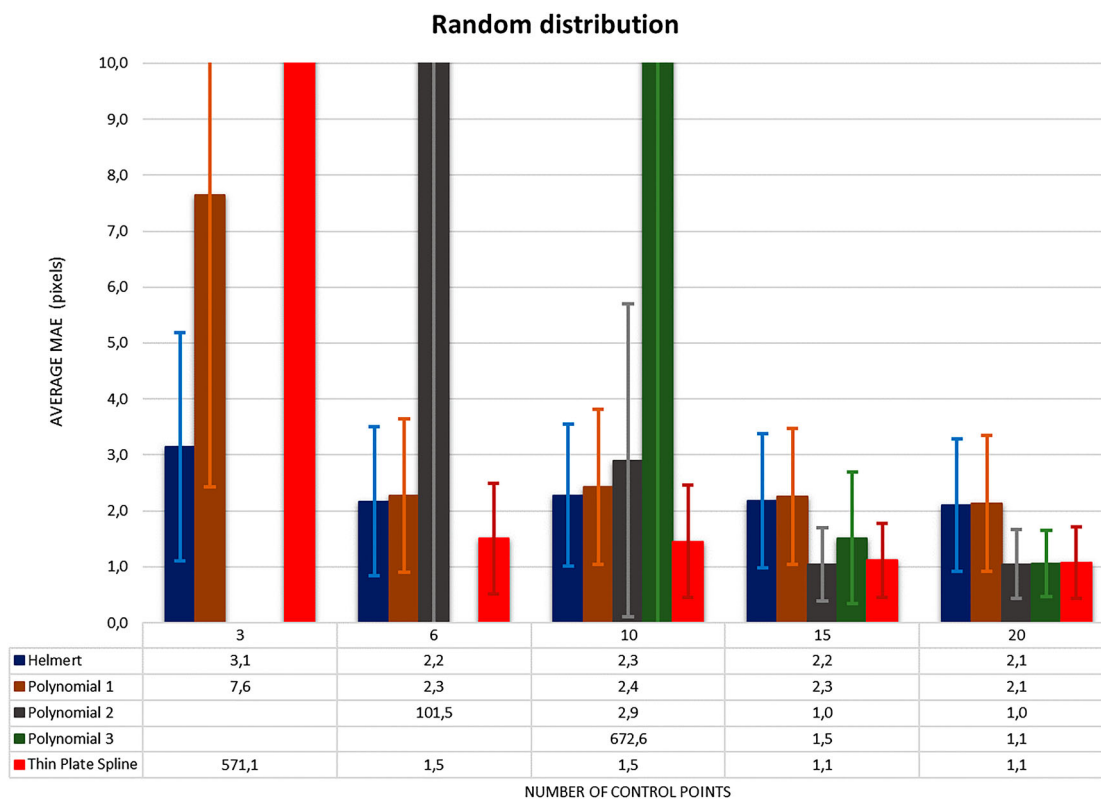


Figure 12. Average MAE and SDAE results for random distribution georeferencing projects.

between 13.4 and 14.0 pixels. In this case, there is a significant reduction for 15 control points with an average MAE of 4.4 pixels and a deviation of 3.9. For the TPS transformation,

the average MAE varies between 3.2 pixels for three control points and 0.9 pixel for 20 control points, with the deviation varying between 2.0 and 0.6 pixels.

Figure 11 represents the results obtained for the stratified distribution georeferencing projects. Thus, for the Helmert transformation, the average MAE varies from 6.5 pixels for three control points to 6.9 pixels for 20 control points, with a deviation of the result varying from 5.6 pixels for three control points to 5.3 pixels for 20 control points. The maximum is found for 10 control points with an average MAE of 7.2 pixels and a deviation of 5.2 pixels. For the P1 transformation, the average MAE varies between 6.2 pixels for three control points and 7.6 pixels for 20 control points, and the deviation varies between 5.3 and 5.7 pixels for three and 20 control points, respectively. The maximum is found for 10 control points with an average MAE of 8.5 pixels and a deviation of 5.9 pixels. For the P2 transformation, the average MAE varies between 73.3 pixels for six control points and 19.7 pixels for 20 control points, with the deviation varying between 75.7 and 16.2 pixels. For the P3 transformation, the average MAE varies between 14471.0 pixels for 10 control points and 79.4 pixels for 20 control points, and the deviation varies between 16311.7 and 83.8 pixels. For the TPS transformation, the average MAE varies between 6.2 pixels for three control points and 8.3 pixels for 20 control points, with the deviation varying between 5.3 and 5.9 pixels. The maximum is reached for 15 control points with an average MAE of 9.7 pixels and a deviation of 6.8 pixels.

Figure 12 represents the results obtained for the random distribution georeferencing projects. Thus, for the Helmert transformation, the average MAE varies from 3.1 pixels for three control points to 2.1 pixels for 20 control points, with a deviation of the result varying from 2.0 pixels for three control points to 1.2 pixels for 20 control points. For the P1 transformation, the average MAE varies between 7.6 pixels for three control points and 2.1 pixels for 20 control points, and the deviation varies between 5.2 and 1.2 pixels for three and 20 control points, respectively. For the P2, the average MAE varies between 101.5 pixels for six control points and 1.0 pixels for 20 control points, with the deviation varying between 118.8 and 0.6 pixels. For the P3 transformation, the average MAE varies between 672.6 pixels for 10 control points and 1.1 pixels for 20 control points, and the deviation varies between 893.3 and 0.6 pixels. For the TPS transformation, the average MAE varies between 571.1 pixels for three control points and 1.1 pixels for 20 control points, with the deviation varying between 388.3 and 0.6 pixels.

## Discussion

If we analyse the results according to the type of transformation used, we see that the best results are obtained for TPS transformation. However, there is an important nuance in the case of using only three control points since the MAE increases, especially if the combination of the control points is not adequate. For this type of transformation and the edge and stratified distributions, the results are very even, with an MAE ranging between 0.9 and 1.3 pixels and deviations between 0.6 and 0.8 pixels. For the corner distribution, the values are in the order of three times higher with

an MAE between 6.1 and 9.7 pixels and deviations between 5.4 and 6.8 pixels. For the random distribution and three control points, an anomalous value appears due to the poor result obtained in one of the five repetitions of this type of georeferencing project. The suitability of the TPS transformation versus polynomial methods has already been reported by (Pedersen 2000) in the registrations of 2D gel electrophoresis images. For the Helmert transformation, very even values are obtained for all distributions, except for the corner distribution where the values approximately triple. Thus the MAE values range between 2.0 and 3.1 pixels with deviations of 1.1 and 2.0 pixels. However, in the corner distribution, these values rise to an MAE of 7.2 pixels and a deviation of 5.2 pixels. Even so, the values are almost double those obtained by TPS transformation, although this transformation method should be used when no deformations are to be introduced in the transformed image (Boutoura and Livieratos 2006).

The results obtained for the P1 transformation are similar to those obtained by Helmert, but they are somewhat higher. The MAE values range from 2.0 for the edge distribution to 8.5 for the corner distribution, with deviations of 1.2 and 5.9, respectively. The results obtained for the P2 transformations worsen those obtained for P1 when the number of control points used is low. From 10 control points onwards, the results are similar to those obtained by Helmert and the P1 transformation, and for 20 control points they become similar to those obtained by TPS transformation. The suitability of grade two for the polynomial transformations has also been contrasted in other studies (Mohammed et al. 2013). However, the P2 transformation is heavily penalised for the corner distribution, with MAE values up to 106.1 pixels and deviations of 92.3 pixels. The results obtained by the P3 transformation worsen the results obtained by P2's transformation. Thus, even for 20 control points and edge distribution, the MAE amounts to 4.1 pixels with a deviation of 2.6. For this type of transformation, good results have only been obtained for 15–20 control points and random distribution. This fact contrasts with those obtained by (Baiocchi et al. 2013), who obtained better results with P3 compared to P2 for georeferencing a historical map of Rome.

By analysing the results according to the type of distribution, we can see that the best results have been obtained for the edge and stratified distributions. From six control points onwards, similar results are also obtained for the random distribution. Thus, for the edge and stratified distributions, not including the P3 transformation results, the MAE values range between 4.3 and 1.0 pixels with a deviation between 2.5 and 0.6 pixels. Clearly, the worst results are obtained for the corner distribution where for the P3 transformation the average MAE value amounts to 14471.0 pixels and a deviation of 16311.7 pixels with an MAE minima of 79.4 and 83.8 pixels deviation. Therefore, this type of distribution is not feasible. Even for the TPS transformation the average MAE value amounts to 9.7 pixels, which may be too high for the vast majority of engineering applications. This agrees with the results of (Zhou and Li 2000), who indicate that a dense but sparsely spread

control point distribution performs worse than a less dense but better spread distribution. Regardless of the type of transformation, a random distribution can be effective if a minimum of about 15 control points is used, but if the number of control points used is low, it can lead to high MAE errors. This is explained by the fact that as the number of control points increase, the control point distribution is more likely to be well spread.

With some exceptions, increasing the number of control points improves the accuracy of the results, regardless of the type of transformation and the type of distribution, a fact that has been previously evidenced by other authors in the scientific literature (Zhou and Li 2000). In fact, the use of only three control points only gives approximately constant results for the Helmert distribution. In this case, the three control points should be placed as far apart as possible (Watson 2006). From 10 control points onwards, the improvement stabilises even if the number of control points is increased. The results remain approximately stable.

## Conclusions

Monitoring the regeneration process of a forest is an important part of forestry management. Compared to the traditional methods of counting tree species, UAVs have been a revolutionary means of saving time and costs due to the temporal and spatial flexibility of the data collection. In turn, the integration of multispectral cameras allows the traditional vegetation indices that have been used with satellite imagery to be obtained. However, data from multispectral cameras must be combined with data from other types of sensors, such as RGB. It is therefore necessary to co-register all the information in order to obtain combined vegetation indices and carry out segmentation processes that allow the identification of the different tree species. In order to carry out this co-registration, easily accessible GIS tools, such as QGIS, can be used. This software has a georeferencing tool with different transformation methods; however, not all of them allow the co-registration of the data to be obtained with the same level of precision. Regardless of the type of transformation, it is possible to obtain accuracy levels with an MAE of around 3–4 pixels and deviations of 2–3 pixels. However, to improve this result, it is necessary to define a suitable number and the distribution of control points. Thus, in this study, the best results have been obtained for the TPS transformation from 10 control points and with edge or stratified distribution. Similar data have also been obtained with the second-degree polynomial transformation, but, in this case, with a larger number of control points. This research article is the first step to continue advancing in future research on automatic counts and identification of tree species from multispectral images captured from a UAV.

## Acknowledgements

Thanks to the Department of Forestry and Wildlife Management of the Inland Norway University of Applied Sciences (Evenstad, Norway) for

participating in the initial approach to the problem studied and for facilitating access to the study area.

## Disclosure statement

No potential conflict of interest was reported by the author(s).

## Data availability statement (DAS)

The data that support the findings of this study are openly available in “figshare” at <https://doi.org/10.6084/m9.figshare.14350655>

## ORCID

Patricio Martínez-Carricondo  <http://orcid.org/0000-0001-9556-7998>  
 Fernando Carvajal-Ramírez  <http://orcid.org/0000-0001-7791-0991>  
 Francisco Agüera-Vega  <http://orcid.org/0000-0003-0709-3388>

## References

- Agarwal S, Vailshery L, Jaganmohan M, Nagendra H. 2013. Mapping Urban tree species using very high resolution satellite imagery: comparing pixel-based and object-based approaches. *ISPRS Int J Geoinf.* 2(1):220–236. doi:10.3390/ijgi2010220.
- Agüera-Vega F, Carvajal-Ramírez F, Martínez-Carricondo P. 2017. Accuracy of digital surface models and orthophotos derived from unmanned aerial vehicle photogrammetry. *Journal of Surveying Engineering* 143. 04016025. doi:10.1061/(ASCE)SU.1943-5428.0000206.
- Baiocchi V, Lelo K, Milone MV, Mormile M. 2013. Accuracy of different georeferencing strategies on historical maps of Rome. *Geographia Technica* (1):10–16.
- Bartoli A, Perriollat M, Chambon S. 2010. Generalized thin-plate spline warps. *Int J Comput Vision.* doi:10.1007/s11263-009-0303-4.
- Bookstein FL. 1989. Principal warps: thin-plate splines and the decomposition of deformations. *IEEE Trans Pattern Anal Mach Intell* 11, 567–585. doi:10.1109/34.24792.
- Boutoura C, Livieratos E. 2006. Some fundamentals for the study of the geometry of early maps by comparative methods. *E-Perimtron.* 1 (1):60–70.
- Brigante R, Radicioni F. 2014. Georeferencing of historical maps: Gis technology for urban analysis. *Geographia Technica.* 09(1):10–19.
- Brown LG. 1992. A survey of image registration techniques. *ACM Comput Surv* 24, 325–376. doi:10.1145/146370.146374.
- Cajtham J. 2011. Methods of georeferencing old maps on the example of Czech early maps. In *Proceedings of the 25th International Cartographic Conference.*
- Chen S, McDermid GJ, Castilla G, Linke J. 2017. Measuring vegetation height in linear disturbances in the boreal forest with UAV photogrammetry. *Remote Sens (Basel)* 9, 1257. doi:10.3390/rs9121257.
- Dandois JP, Olano M, Ellis EC. 2015. Optimal altitude, overlap, and weather conditions for computer vision uav estimates of forest structure. *Remote Sens (Basel).* 7(10):13895–13920. doi:10.3390/rs71013895.
- Dawn S, Saxena V, Sharma B. 2010. Lecture notes in computer science. In *Lecture Notes in Computer Science (Including Subseries Lecture Notes in Artificial Intelligence and Lecture Notes in Bioinformatics).* 6134, 103–112. doi:10.1007/978-3-642-13681-8\_13.
- Dias JD, Backes AR, Escarpinati MC. 2019. Detection of control points for UAV-multispectral sensed data registration through the combining of feature descriptors. In *VISIGRAPP 2019 - Proceedings of the 14th International Joint Conference on Computer Vision, Imaging and Computer Graphics Theory and Applications (Vol. 4),* 444–451. doi:10.5220/0007580204440451.
- Domingo D, Ørka HO, Næsset E, Kachamba D, Gobakken T. 2019. Effects of UAV image resolution, camera type, and image overlap on accuracy

- of biomass predictions in a tropical woodland. *Remote Sens (Basel)*, 948. 11(8). doi:10.3390/rs11080948
- Donato G, Belongie S. 2002. Lecture notes in computer science. In *Lecture Notes in Computer Science (Including Subseries Lecture Notes in Artificial Intelligence and Lecture Notes in Bioinformatics)*. 2352, 21–31. doi:10.1007/3-540-47977-5\_2.
- Feduck C, McDermid GJ, Castilla G. 2018. Detection of coniferous seedlings in UAV imagery. *Forests* 9, 432. doi:10.3390/f9070432.
- Follin J-M, Fahrasmann M, Simonetto É. 2016. An open-source based tool-chain for the georeferencing of old cadastral maps. *PeerJ*. 4:2222v3. doi:10.7287/peerj.preprints.2222.
- Fonstad MA, Dietrich JT, Courville BC, Jensen JL, Carbonneau PE. 2013. Topographic structure from motion: A new development in photogrammetric measurement. *Earth Surf Processes Landforms* 38, 421–430. doi:10.1002/esp.3366.
- Franklin SE, Hall RJ, Smith L, Gerylo GR. 2003. Discrimination of conifer height, age and crown closure classes using landsat-5 TM imagery in the Canadian northwest territories. *Int J Remote Sens* 24, 1823–1834. doi:10.1080/01431160210144589.
- Fritz A, Kattenborn T, Koch B. 2013. UAV-based photogrammetric point clouds – tree stem mapping in open stands in comparison to terrestrial laser scanner point clouds. *The International Archives of the Photogrammetry, Remote Sensing and Spatial Information Sciences*, 141–146. doi:10.5194/isprsarchives-xl-1-w2-141-2013.
- Furukawa Y, Ponce J. 2010. Accurate, dense, and robust multiview stereopsis. *IEEE Trans Pattern Anal Mach Intell*. 32(8):1362–1376. doi:10.1109/TPAMI.2009.161.
- Gomes MF, Maillard P. 2016. Environmental applications of remote sensing. In *Environmental Applications of Remote Sensing*. doi:10.5772/62122.
- Goodbody TRH, Coops NC, Hermosilla T, Tompalski P, Crawford P. 2018. Assessing the status of forest regeneration using digital aerial photogrammetry and unmanned aerial systems. *Int J Remote Sens* 39, 5246–5264. doi:10.1080/01431161.2017.1402387.
- Gougeon FA. 1995. A crown-following approach to the automatic delineation of individual tree crowns in high spatial resolution aerial images. *Can J Remote Sens* 21, 274–284. doi:10.1080/07038992.1995.10874622.
- Hall RJ, Aldred AH. 2014. Forest regeneration appraisal with large-scale aerial photographs. *The Forestry Chronicle* 68, 142–150. doi:10.5558/tfc68142-1.
- Hentz ÁMK, Dalla Corte AP, Netto SP, Strager MP, Schoeninger ER. 2018. Treedetection: automatic tree detection using UAV-based data. *Floresta*. 48(3). doi:10.5380/rf.v48i3.56150
- Hird JN, Montaghi A, McDermid GJ, Kariyeva J, Moorman BJ, Nielsen SE, McIntosh ACS. 2017. Use of unmanned aerial vehicles for monitoring recovery of forest vegetation on petroleum well sites. *Remote Sens (Basel)* 9, 413. doi:10.3390/rs9050413.
- Hirschmugl M, Ofner M, Raggam J, Scharadt M. 2007. Single tree detection in very high resolution remote sensing data. *Remote Sens Environ* 110, 533–544. doi:10.1016/j.rse.2007.02.029.
- Jaskierniak D, Kuczera G, Benyon R, Wallace L. 2015. Using tree detection algorithms to predict stand sapwood area, basal area and stocking density in eucalyptus regnans forest. *Remote Sens (Basel)* 7, 7298–7323. doi:10.3390/rs70607298.
- Jhan JP, Rau JY, Huang CY. 2016. Band-to-band registration and orthorectification of multilens/multispectral imagery: A case study of MiniMCA-12 acquired by a fixed-wing UAS. *ISPRS J Photogramm Remote Sens* 114, 66–77. doi:10.1016/j.isprsjprs.2016.01.008.
- Kang J, Wang L, Chen F, Niu Z. 2017. Identifying tree crown areas in undulating eucalyptus plantations using JSEG multi-scale segmentation and unmanned aerial vehicle near-infrared imagery. *Int J Remote Sens* 38, 2296–2312. doi:10.1080/01431161.2016.1253900.
- Ke Y, Quackenbush LJ. 2011. A comparison of three methods for automatic tree crown detection and delineation from high spatial resolution imagery. *Int J Remote Sens* 32, 3625–3647. doi:10.1080/01431161003762355.
- Keller W, Borkowski A. 2019. Thin plate spline interpolation. *J Geod* 93, 1251–1269. doi:10.1007/s00190-019-01240-2.
- Leckie DG, Gougeon F, McQueen R, Oddleifson K, Hughes N, Walsworth N, Gray S. 2017. Production of a large-area individual tree species Map for forest inventory in a complex forest setting and lessons learned. *Can J Remote Sens* 43, 140–167. doi:10.1080/07038992.2017.1286974.
- Martínez-Carricondo P, Agüera-Vega F, Carvajal-Ramírez F, Mesas-Carrascosa FJ, García-Ferrer A, Pérez-Porrás FJ. 2018. Assessment of UAV-photogrammetric mapping accuracy based on variation of ground control points. *Int J Appl Earth Obs Geoinf*. 72(February):1–10. doi:10.1016/j.jag.2018.05.015.
- Mohammed NZ, Eisa E, Elhaj A. 2013. The effect of polynomial order on georeferencing remote sensing images. *Certified International Journal of Engineering and Innovative Technology*. 2(8):1–4.
- Nevalainen O, Honkavaara E, Tuominen S, Viljanen N, Hakala T, Yu X, ... Tommaselli AMG. 2017. Individual tree detection and classification with UAV-based photogrammetric point clouds and hyperspectral imaging. *Remote Sens (Basel)* 9, 185. doi:10.3390/rs9030185.
- Panagiotidis D, Abdollahnejad A, Surovó P, Chiteculo V. 2017. Determining tree height and crown diameter from high-resolution UAV imagery. *Int J Remote Sens* 38, 2392–2410. doi:10.1080/01431161.2016.1264028.
- Pedersen L. 2000. Estimation OF THIN PLATE SPLINE WARP PARAMETERS FROM PROTEIN SPOT POSITIONS IN 2D ELECTROPHORESIS GELS. *Math Model*.
- Peña JM, Torres-Sánchez J, Serrano-Pérez A, de Castro AI, López-Granados F. 2015. Quantifying efficacy and limits of unmanned aerial vehicle (UAV) technology for weed seedling detection as affected by sensor resolution. *Sensors* 15, 5609–5626. doi:10.3390/s150305609.
- Pérez J. 2001. Apuntes e fotogrametría III. UNIVERSIDAD DE EXTREMADURA CENTRO UNIVERSITARIO DE MÉRIDA.
- Pouliot DA, King DJ, Pitt DG. 2005. Development and evaluation of an automated tree detection-delineation algorithm for monitoring regenerating coniferous forests. *Can J For Res* 35, 2332–2345. doi:10.1139/x05-145.
- Puliti S, Ørka HO, Gobakken T, Næsset E. 2015. Inventory of small forest areas using an unmanned aerial system. *Remote Sens (Basel)* 7, 9632–9654. doi:10.3390/rs70809632.
- Puliti S, Talbot B, Astrup R. 2018. Tree-stump detection, segmentation, classification, and measurement using unmanned aerial vehicle (UAV) imagery. *Forests* 9, 102. doi:10.3390/f9030102.
- Rouse JW, Haas RH, Schell JA, Deering DW, Harlan JC. 1974. Monitoring the vernal advancements and retrogradation of natural vegetation. Texas A&M University. Remote Sensing Center. College Station.
- Sprengel R, Rohr K, Stiehl HS. 1997. Thin-plate spline approximation for image registration. In *Annual International Conference of the IEEE Engineering in Medicine and Biology - Proceedings*. doi:10.1109/iembs.1996.652767.
- Turner D, Lucieer A, Malenovsky Z, King DH, Robinson SA. 2014. Spatial co-registration of ultra-high resolution visible, multispectral and thermal images acquired with a micro-UAV over antarctic moss beds. *Remote Sens (Basel)*. 6(5), 4003–4024. doi:10.3390/rs6054003
- Vauhkonen J, Ene L, Gupta S, Heinzel J, Holmgren J, Pitkänen J, ... Maltamo M. 2012. Comparative testing of single-tree detection algorithms under different types of forest. *Forestry*. 85(1), 27–40. doi:10.1093/forestry/cpr051
- Wallace L, Lucieer A, Watson CS. 2014. Evaluating tree detection and segmentation routines on very high resolution UAV LiDAR data. *IEEE Trans Geosci Remote Sens* 52, 7619–7628. doi:10.1109/TGRS.2014.2315649.
- Wallace L, Musk R, Lucieer A. 2014. An assessment of the repeatability of automatic forest inventory metrics derived from UAV-borne laser scanning data. *IEEE Trans Geosci Remote Sens* 52, 7160–7169. doi:10.1109/TGRS.2014.2308208.
- Watson GA. 2006. Computing helmert transformations. *J Comput Appl Math* 197, 387–394. doi:10.1016/j.cam.2005.06.047.
- Widyaningrum E, Fajari M, Octariady J. 2016. <![CDATA[ACCURACY COMPARISON OF VHR SYSTEMATIC-ORTHO SATELLITE IMAGERIES AGAINST VHR ORTHORECTIFIED IMAGERIES USING GCP]]>. *ISPRS - International Archives of the Photogrammetry, Remote Sensing and Spatial Information Sciences*, 305–309. doi:10.5194/isprsarchives-XLI-B1-305-2016.
- Willmott CJ, Matsuura K. 2005. Advantages of the mean absolute error (MAE) over the root mean square error (RMSE) in assessing average model performance. *Clim Res* 30, 79–82. doi:10.3354/cr030079.

- Willneff J, Weser T, Rottensteiner F, Fraser CS. 2008. Precise georeferencing of cartosat imagery Via different orientation models. The International Archives of the Photogrammetry, Remote Sensing and Spatial Information Science. Vol. XXXVII:Part B1.
- Wolf BM, Heipke C. 2007. Automatic extraction and delineation of single trees from remote sensing data. Mach Vis Appl 18, 317–330. doi:10.1007/s00138-006-0064-9.
- Wulder M, Niemann KO, Goodenough DG. 2000. Local maximum filtering for the extraction of tree locations and basal area from high spatial resolution imagery. Remote Sens Environ 73, 103–114. doi:10.1016/S0034-4257(00)00101-2.
- Zhou G, Li R. 2000. Accuracy evaluation of ground points from IKONOS high-resolution satellite imagery. Photogramm Eng Remote Sensing. 66(9):1103–1112.